



Deposited via The University of Sheffield.

White Rose Research Online URL for this paper:

<https://eprints.whiterose.ac.uk/id/eprint/165355/>

Version: Accepted Version

Article:

Neto, M.Q. and Rainforth, W.M. (2020) Effect of potential and microstructure on the tribocorrosion behaviour of beta and near beta Ti alloys I. *Biotribology*, 24. 100141. ISSN: 2352-5738

<https://doi.org/10.1016/j.biotri.2020.100141>

Article available under the terms of the CC-BY-NC-ND licence
(<https://creativecommons.org/licenses/by-nc-nd/4.0/>).

Reuse

This article is distributed under the terms of the Creative Commons Attribution-NonCommercial-NoDerivs (CC BY-NC-ND) licence. This licence only allows you to download this work and share it with others as long as you credit the authors, but you can't change the article in any way or use it commercially. More information and the full terms of the licence here: <https://creativecommons.org/licenses/>

Takedown

If you consider content in White Rose Research Online to be in breach of UK law, please notify us by emailing eprints@whiterose.ac.uk including the URL of the record and the reason for the withdrawal request.

Effect of potential and microstructure on the tribocorrosion behaviour of beta and near beta Ti alloys I

M. Queiroz Neto, WM Rainforth

Department of Materials Science and Engineering, University of Sheffield, Sir Robert Hadfield Building, Mappin Street, Sheffield, S1 3JD, UK

Abstract

Current hip prostheses make extensive use of the aerospace alloy Ti-6Al-4V. This material was designed for aerospace applications but has far from ideal mechanical properties for biomedical applications, namely, a high elastic modulus and poor fatigue resistance. Moreover, its poor tribological properties are well known. However, beta, or near beta Ti alloys are known to have superior properties in that its elastic modulus is closer to that of bone coupled with a good fatigue resistance. Therefore, this work aims to analyse the tribocorrosion behaviour of 4 different titanium alloys (Ti-13Nb-13Zr, Ti-12Mo-6Zr-2Fe and Ti-29Nb-13Ta-4.6Zr aged at 300°C and at 400°C) at anodic potential, OCP and cathodic potential at 0.5N, 1N and 2N in bovine serum to identify the main cause of material degradation, the presence of a tribofilm and the synergism between corrosion and wear. The results show the alloys become more active when subjected to sliding in all conditions, but the material loss is lower at anodic potential. The alloys studied present a positive effect of corrosion on wear.

Introduction

The titanium alloy Ti6Al4V is the most common alloy used in components for total hip replacements [1]. It provides better corrosion resistance and osseointegration properties than CoCrMo or stainless steel [2]. Ti6Al4V alloy has established itself as the standard for femoral stems and acetabular cups [3-5]. Recent reports of adverse local tissue reactions (ALTR) due to taper corrosion have led to a further decline in the use of CoCrMo alloy for femoral stems and an increase of Ti6Al4V alloy. Yet, ALTR can occur in titanium stems coupled with CoCrMo femoral heads, and even in rare cases when coupled with ceramic heads [6]. Recently, a beta phase titanium alloy (TMZF) was introduced to provide better stress shielding properties and thus

increased osseointegration [7]. However, implants made from TMZF showed in some cases gross trunnion failure (GTF) [8-12]. This failure mode led to an excessive release of titanium alloy debris and in some cases disengagement of the head from the stem. The reason for GTF is multifactorial including material properties, surface roughness, implant design, and femoral off-set (unfavourable moment arm) [8, 12, 13]. Even though the use of TMZF for femoral stems has been discontinued, lessons learned can be applied to develop new alloys that provide improved tribocorrosion and fretting corrosion properties, decreased reduce stress shielding, and equal or better cyclic fatigue properties [14-19]. By doing so, it is of utmost importance to pay close attention to the implant alloy microstructure which can vary broadly even at the same chemical composition depending on the heat treatment and thermomechanical processing applied [20-23].

It was the goal of this study a) to produce four different types of titanium alloy with distinctively different microstructures with lower elastic moduli and reduced amount of potentially toxic elements compared to Ti6Al4V, and b) to investigate the tribocorrosion properties of these alloys. Specifically Ti-13Nb-13Zr, Ti-29Nb-13Ta-4.6Zr, Ti-29Nb-13Ta-4.6Zr aged at 300°C and Ti-29Nb-13Ta-4.6Zr aged at 400°C where investigated. The tribocorrosion behaviour was evaluated at three different loads, three different potentiostatic conditions, and the synergistic effect between wear and corrosion was evaluated using two different models.

Methods

All beta titanium alloys were produced in a vacuum arc melting furnace using an Arc 200 arc melter supplied by Arcast. Alloying elements for each alloy were melted with a DC transferred arc as the heat source. A hundred grams of material was melted for each alloy composition. The machine was evacuated and flooded with argon.

After melting and casting, all samples were heat treated at 1000°C for 4 hours in an argon tubular furnace in order to homogenise, to remove microscale concentration gradients, and to obtain a uniform composition throughout the ingot.

Ti-13Nb-13Zr was subjected to a reduction of 67% by hot rolling at 680°C. Subsequently, it was solution treated at 760°C for 1 hour and water quenched. Ti-

12Mo-6Zr-2Fe alloy was hot rolled (65% reduction), then aged at 600°C for 4 hours and air cooled. The β transus temperature of this alloy is 743°C.

Ti-29Nb-13Ta-4.6Zr was cold rolled to 87% reduction. Then it was solution treated at 790°C for 1 hour followed by water quenching. Furthermore, this alloy was divided in two groups. The first group was aged at 400°C for 72 hours and water quenched, whereas the second group was aged at 300°C for 72 hours followed by water quenching. The β transus temperature of both alloys is 740°C.

Microstructural analysis

Phase volume fraction was determined on bulk alloy samples that were polished and viewed by scanning electron microscopy (SEM) using the backscatter electron (BSE) mode. Different phases could be distinguished by contrast based on the atomic number of the alloying elements present within each phase. For X-ray diffraction (XRD) a Bruker D2 Phaser was used to characterize the lattice structure of different phases present within each alloy.

Surface analysis

The initial surface of all samples was characterized by SEM (FEI, InspectF, Netherlands) and optical profilometry (Contour GT 3D Optical Microscope, Bruker, UK) was performed to measure the surface roughness. Profilometry was also used to assess the wear scar profile of the specimens after testing.

Electrochemical measurements

The polarization behaviour of all alloys was measured in an electrochemical cell consisting of a container with a Ag/AgCl 1M KCl reference electrode (potential with respect to the standard hydrogen electrode is 0.235V) and a platinum wire as a counter electrode. The exposed areas were 1.54 cm². Polarization curves were measured using a VersaSTAT 3F Ametek potentiostat connected to the VersaStudio software. The potential scanning range was from -0.25V to 0.25V vs OCP at a sweep rate of 0.5 mV/s. Tests were started after potential stabilization period of 15 minutes. Two types of test were conducted: 1) under static conditions, 2) under sliding conditions. The corrosion potential was determined under each condition using the Tafel's method.

Tribocorrosion tests

Reciprocating sliding wear tests were carried out using a Bruker UMT Multi Specimen Test System (Bruker, UK) controlled by CETR UMT software. A ball on plate configuration according to ASTM G133 was used. The counter body was an alumina ball with 4 mm diameter and 99% purity (Oakwade Ltd., UK). An alumina ball was used to provide an inert counter face and to be able to compare the current tests with previous published work. New-born calf serum (First Link (UK) Ltd.) was used to simulate body fluids. It was diluted to 25 vol% in an aqueous solution of phosphate buffer saline (Sigma-Aldrich). One wt% sodium azide (99% extra pure, ArcosOrganics) was added to the solution to avoid bacterial growth. The final testing solution had a protein content of 15.5 g/L. A stroke of 2mm at 5 Hz (0.02 m/s) was used for the reciprocating tribocorrosion test. The test duration was 3h in all cases (54,000 cycles/ 216 m sliding distance). The normal load (Hertzian contact pressure) was 0.5N (521 MPa), 1N (657 MPa) and 2N (827 MPa). Tribocorrosion tests were performed at a cathodic potential (-1V vs OCP) and an anodic potential (0.3V vs OCP). The potentials were chosen according to ASTM G119.09 for synergy estimation. Also, potentiodynamic polarization tests were performed during the reciprocating sliding test. Tests were performed in duplicate for each alloy to test the reproducibility.

Synergy estimations

The synergism between corrosion and wear on tribocorrosion can be estimated by several ways. This study used two approaches: the synergistic approach [24] and mechanistic approach [25]. The synergistic approach is expressed by equation 1. Each component of equation 1 was found using ASTM G119.09 standard.

$$T = W_o + C_o + \Delta W_c + \Delta C_w \quad \text{Eq. 1}$$

T: Total material loss; W_o : Material loss due to wear; C_o : Material loss due to corrosion; W_c : The increase of wear due to corrosion and C_w : The increase of corrosion due to wear.

In the mechanistic approach, the material loss is due to mechanical wear where the material will be worn due to mechanical contact, and wear accelerated corrosion where the area exposed by the mechanical contact will be more reactive. This approach is expressed by the equation 2.

$$V_t = V_{mec} + V_{chem} \quad \text{Eq. 2}$$

Where V_t is the total material loss, V_{mech} is the material loss due to mechanical wear and V_{chem} is the material loss due to corrosion. Using Faraday's law, the materials loss due to corrosion is found using the following equation.

$$V_{chem} = \frac{i \times t \times M}{n \times F \times \rho} \quad \text{Eq. 3}$$

Results

Materials characterization

The Ti-13Nb-13Zr alloy was a $\alpha\beta$ alloy with a martensitic microstructure in a β matrix (Fig. 1 (a)) and an average grain size of 140 μm . The phase content was 47.2% α and 52.8% β phase. X-ray diffraction (Fig. 2) confirmed the presence of β and α'' phases which is the most intense peak seen for α'' (112). The microstructure of Ti-12Mo-6Zr-2Fe was characterized by fine grains (Fig. 1 (b)) with an average grain size of 1.6 μm both α and β phase. The phase content was 39.1% α and 60.9% β phase, which is considered a near β alloy. X-ray diffraction confirmed the presence of β phase as well as a low intensity (110) peak of the α phase (Figure 2).

The microstructure of Ti-29Nb-13Ta-4.6Zr aged at 400°C had an average grain size of 20 μm (Figure 1 (c)) and the microstructure of Ti-29Nb-13Ta-4.6Zr alloy aged at 300°C (Figure 1 (d)) had an average grain size of 12.8 μm . Both alloys had an equiaxed β grain structure due to the heat treatment at the β domain, recrystallization and grain growth. Based on the SEM images both alloys exhibited a volume fraction of 100% β phase. However, ω phase could not be differentiated by BSE, but was identified only in this alloy by XRD. ω phase transformation is induced by aging at a low temperature. The ω phase volume fraction could not be assessed. X-ray diffraction confirmed a β microstructure for the alloy aged at 400°C (Figure 2), whereas at 300°C β and ω —indicated by the (112) peak—phases occurred. The low intensity of ω phase is expected, since this phase is known to occur in small fractions after aging.

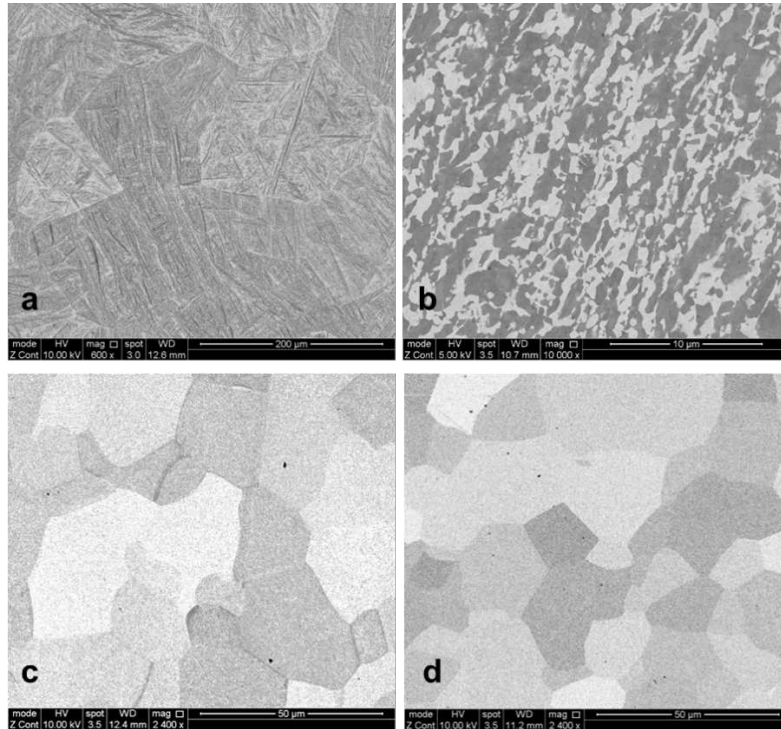


Fig. 1 – (a) SEM backscatter electron image of the $\alpha\beta$ alloy microstructure, (b) SEM backscatter electron image of the $N\beta$ alloy microstructure, (c) SEM backscatter electron image of the β alloy microstructure and (d) SEM backscatter electron image of the $\beta\omega$ alloy microstructure

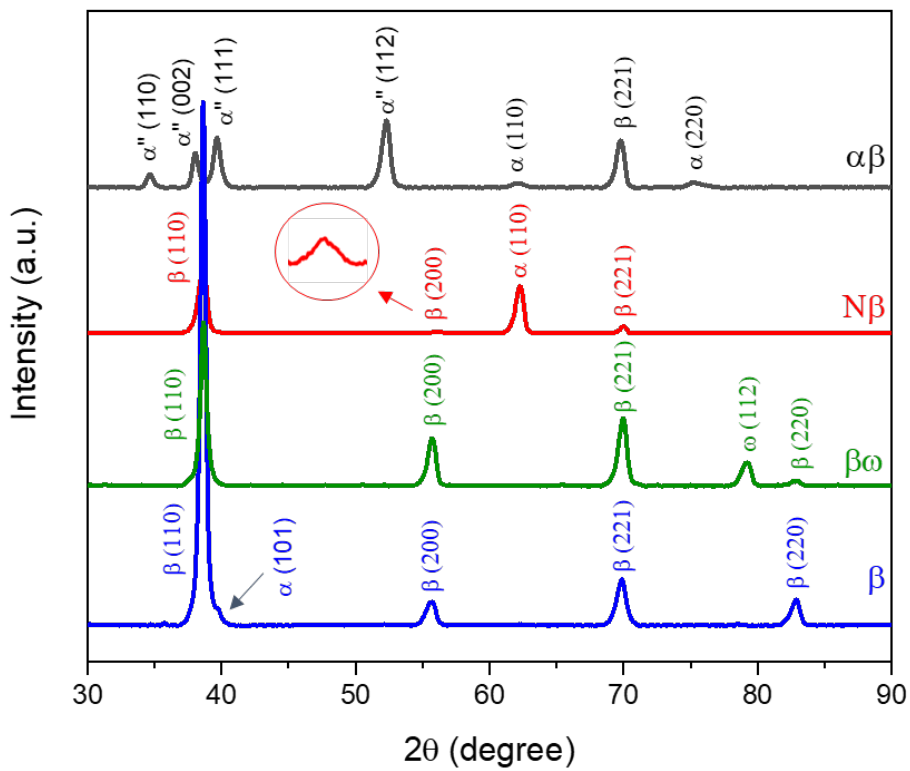


Fig. 2 - X-ray diffraction of the alloys studied in this study.

Corrosion potential

For all materials, it was observed that the potential dropped to more active values and the corrosion current increased under sliding due to the effect of wear on corrosion (Figure 2, Table 1). The corrosion potential before sliding was -0.49V and dropped to -0.96V under sliding for $\alpha\beta$ alloy. The same was observed for the corrosion current, where it was $8.21 \cdot 10^{-9} \text{ A/cm}^2$ under static conditions and increased to $6.66 \cdot 10^{-7} \text{ A/cm}^2$ under sliding condition.

For the $N\beta$ alloy, corrosion potential was -0.52V and dropped to -1.11V under sliding condition. A change in corrosion current was also observed which was $3.26 \cdot 10^{-9} \text{ A/cm}^2$ and $6.22 \cdot 10^{-7} \text{ A/cm}^2$ under sliding conditions. The β alloy showed a corrosion potential of -0.71V and a corrosion current of $4.38 \cdot 10^{-9} \text{ A/cm}^2$ under static condition, and a corrosion potential -1.18V and corrosion current $1.14 \cdot 10^{-6} \text{ A/cm}^2$ at sliding conditions. $\beta\omega$ alloy shows a corrosion potential of -0.51V and corrosion current of $2.55 \cdot 10^{-9} \text{ A/cm}^2$ and corrosion potential -0.97V and corrosion current $9.72 \cdot 10^{-7} \text{ A/cm}^2$ at sliding conditions.

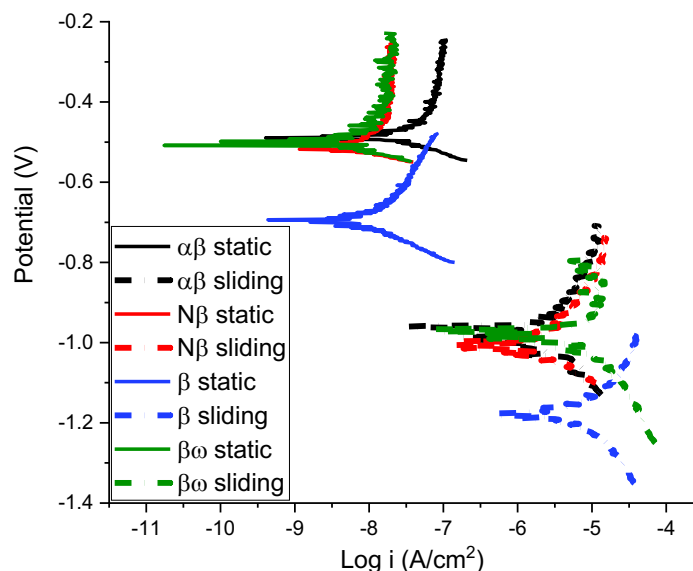


Fig. 3 – Potentiodynamic curves

Table 1 – Corrosion potential and corrosion current.

| Alloys | E _{corr} Static (V) | E _{corr} Sliding (V) | I _{corr} Static (A/cm ²) | I _{corr} Sliding (A/cm ²) |
|--------|------------------------------|-------------------------------|---|--|
| αβ | -0.49 | -0.46 | 8.21 10 ⁻⁹ | 6.66 10 ⁻⁷ |
| Nβ | -0.52 | -1.11 | 3.26 10 ⁻⁹ | 6.22 10 ⁻⁷ |
| β | -0.71 | -1.18 | 4.38 10 ⁻⁹ | 1.14 10 ⁻⁶ |
| βω | -0.51 | -0.97 | 2.55 10 ⁻⁹ | 9.72 10 ⁻⁷ |

Tribocorrosion behaviour under potentiostatic conditions

Current and COF during Cathodic tests

For the αβ alloy, a current drop occurred from -110 μA (0.5N), -57 μA (1N), -50 μA (2N) to -175 μA (0.5N), -91 μA (1N) and -75 μA (2N) when sliding started for all normal loads applied, Fig. 4 (a), and it kept decreasing until the end of sliding, but the current increased to values lower than starting surface at cathodic potential. The COF evolution curves, Fig. 4 (b), exhibited a similar behaviour. The COF increase with increasing normal load. Also, a higher COF occurred at the beginning of sliding (0.65 at 0.5N; 0.71 at 1N and 0.74 at 2N), but decreased until it reached a steady state after 8,000s.

For the Nβ alloy, the initial cathodic current was -100 μA at 0.5N, -45 μA at 1N and -55 μA at 2N. The COF showed initial values of 0.42 at 0.5N, 0.45 at 1N and 0.46 at 2N. These values increase with time and no running in period was observed.

The initial current registered at cathodic potential was -34 μA (all normal loads) for the β alloy and -30 μA (0.5N) and -39 μA (1N and 2N) for βω alloy. For the β alloy at 0.5N the current drops during the whole test up to -140 μA. At 1N it drops to -40 μA and at 2N it drops to -60 μA. Then after 2,000s the current stabilized until the end of the test at 1N and 2N. The current increased when sliding ended. For the βω alloy, the current dropped to -32 μA (0.5N), -47 μA (1N) and -52 μA (2N). A steady state was not observed for this alloy and the current increased to values that still remained lower after sliding compared to before sliding. The COF evolution had a similar qualitative behaviour with different values for each alloy, where a steady state is observed from 5,000s. The COF is high at the beginning of sliding and it is higher at 2N (0.85 for β alloy and 0.8 for βω alloy) and lower at 0.5N (0.55 for β alloy and 0.5 for βω alloy). However, it dropped with time and showed final values around 0.4 and 0.45.

Potential and COF during free potential tests

At OCP, Fig. 4 (c), the potential evolution graph showed 3 areas: passivation, depassivation (wear test) and repassivation (end of sliding) for all alloys. The initial potential recorded before sliding for $\alpha\beta$ alloy was -0.26V at 0.5N; -0.34 at 1N and -0.39V at 2N. Then, the potential dropped when sliding started to -0.8V at 0.5N; -1.1V at 1N and 2N, Fig. 8. At 0.5N the cathodic drop was lower ($\Delta E = -0.54V$) than 1N ($\Delta E = -0.76V$) and 2N ($\Delta E = -0.71V$). Then, the OCP value remained constant until the end of the test. The COF evolution at OCP, Fig. 4 (d), had a similar qualitative behaviour to the COF evolution at cathodic potential. It showed initial values of 0.45 at 0.5N; 0.65 at 1N and 0.68 at 2N. The values decreased with time and at 2,000 s where it remained steady, Fig. 9.

The initial potential of $N\beta$ alloy was 0.09V, 0.08V and 0V at 0.5N, 1N and 2N respectively. The potential dropped to -1V when sliding started in all normal and the $\Delta E = -0.91, -0.92V$ and -1V at 0.5N, 1N and 2N respectively. The COF evolution exhibited a variation with time around 0.35 at 0.5N and 0.45 at 1N and 2N which the running in stage is only observed at 0.5N.

The initial potential for β alloy was -0.54V (0.5N and 1N) and -0.59V (2N). Then a cathodic drop when sliding started was observed to -1V (0.5N and 1N) and -1.1V (2N) with a steady potential evolution with time. $\beta\omega$ showed an initial potential of -0.2V (0.5N), -0.25V (1N) and -1.8V (2N) and a cathodic drop to -1V (0.5N) and -1.1V (2N) and then the same steady potential evolution with time was seen. COF evolution showed high values at 2N (0.75 for β alloy and 0.75 for $\beta\omega$ alloy) and lower values at 0.5N (0.45 for both alloys) at the beginning of the test. A transition point is shown at 4,000s, when its curve showed a steady state with values varying from 0.29 to 0.45.

Anodic tests

Fig. 4 (e) shows the current evolution at anodic potential, the initial current was 1×10^{-7} A and a current increase was observed when sliding starts for all alloys. This shows the effect of wear on corrosion. The current increase is higher at 2N and lower at 0.5N. The current decreased and then exhibited a steady curve until sliding ended, when it dropped to 1×10^{-6} A for all alloys. The reactions of this alloy at this potential is suggested as follow: $Ti = Ti^{2+} + 2e^{-}$. The COF evolution, Fig. 4 (f), at this potential

also showed a current drop (1,000s) and then a steady curve around 0.3. The values of COF at this potential were the lowest values observed in this study.

The average COF, Fig. 5, show low values at anodic potential and high values at cathodic potential. Also, it increased with normal load, except at anodic potential. The lowest value observed is at anodic potential at 2N (0.24) $\alpha\beta$ alloy, and the highest value is observed at cathodic potential at 2N (0.52) $N\beta$ alloy.

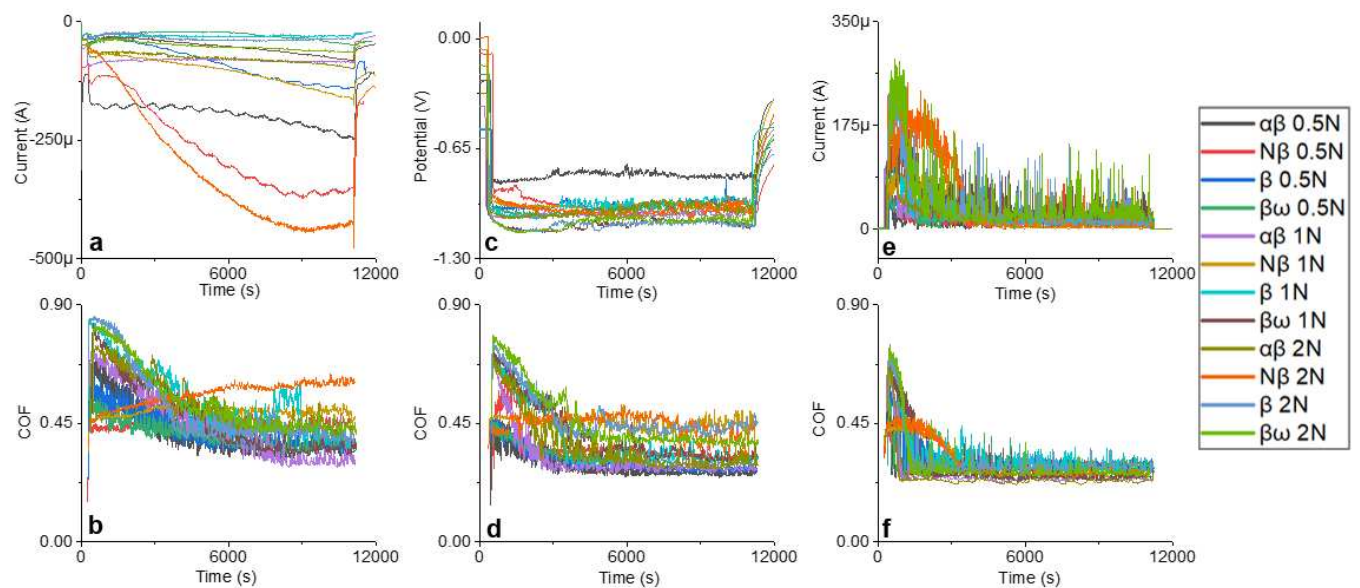


Fig. 4 – (a) Current evolution at cathodic potential, (b) COF evolution at cathodic potential, (c) potential evolution at OCP, (d) COF evolution OCP, (e) current evolution at anodic potential, (f) COF evolution at anodic potential.

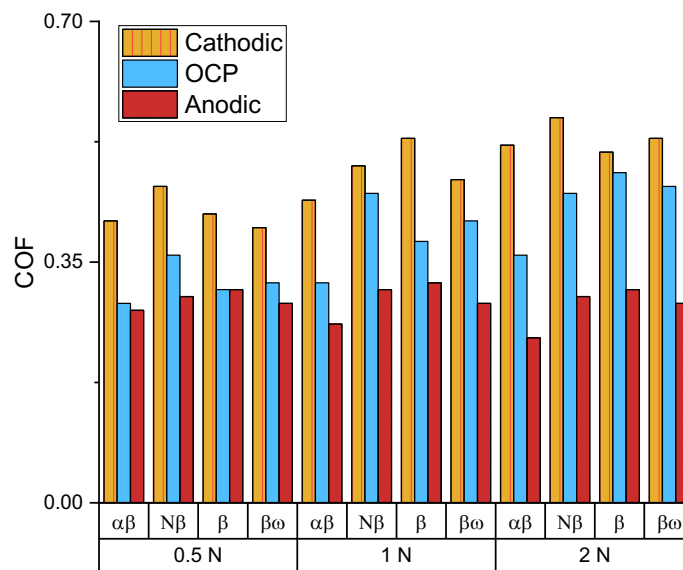


Fig. 5 – Mean COF.

Wear and roughness

The shallowest wear tracks, Fig. 6, were observed at anodic potential and at 0.5N and the deepest wear tracks were observed at cathodic potential and at 2N. For $\alpha\beta$ alloy the shallowest wear track occurred at 0.5N at anodic potential (depth of $35\mu\text{m}$ and a width of 0.71mm) and the deepest wear track was observed at 2N at cathodic potential (depth of $130\mu\text{m}$ and width of 1.2mm). For $N\beta$ alloy, at anodic potential the width and depth varied from 0.8mm and $40\mu\text{m}$ at 0.5N to 1.3mm and $90\mu\text{m}$ at 2N. At cathodic potential the width and depth varied from 1mm and $70\mu\text{m}$ to 1.75mm and $200\mu\text{m}$. The same trend was observed for β and $\beta\omega$ alloys, at anodic potential and 0.5N (depth of $50\mu\text{m}$ for β alloy and $48.5\mu\text{m}$ for $\beta\omega$ alloy).

The wear track volume is illustrated in Figure 6. It also showed lower values at anodic potential and at 0.5N and highest values at 2N at cathodic potential. The worn surface of $\alpha\beta$ alloy at 0.5N at anodic potential had a volume of 0.02mm^3 and the worn surface at 2N at cathodic potential showed a volume of 0.22mm^3 . For $N\beta$ alloy the wear track volume at anodic potential at 0.5N was 0.03mm^3 and at cathodic potential at 2N was 0.3mm^3 . β and $\beta\omega$ alloys, track volume was 0.04 and 0.03mm^3 at anodic potential and 0.30 and 0.29 at cathodic potential respectively.

The specific wear rate, Fig. 7, was also higher at cathodic potential and lower values at anodic potential. However, that showed an increase from 0.5N to 1N and then a drop from 1N to 2N at OCP and cathodic potential. At anodic potential, the specific wear rate decreased with normal load such as for $\alpha\beta$ alloy ($2.29 \cdot 10^{-4} \text{ mm}^3/\text{Nm}$ at 0.5N to $1.19 \cdot 10^{-4} \text{ mm}^3/\text{Nm}$ at 2N). The lowest value of specific wear rate was observed at anodic potential at 2N for $\alpha\beta$ alloy ($1.19 \cdot 10^{-4} \text{ mm}^3/\text{Nm}$) and the highest value was observed at cathodic potential at 1N for $N\beta$ alloy ($9.03 \cdot 10^{-4} \text{ mm}^3/\text{Nm}$ at 1N).

Interestingly, the surface roughness, Fig. 8, was higher at anodic potential, lower at cathodic potential and increased with normal load. The lowest value of surface roughness was observed at anodic potential at 0.5N for $\alpha\beta$ alloy ($0.8\mu\text{m}$) and the highest value was observed at cathodic potential at 2N for $\beta\omega$ alloy ($2.4\mu\text{m}$). The presence of α phase plays the most important factor in this regard and it is attributed to the nature of HCP crystal.

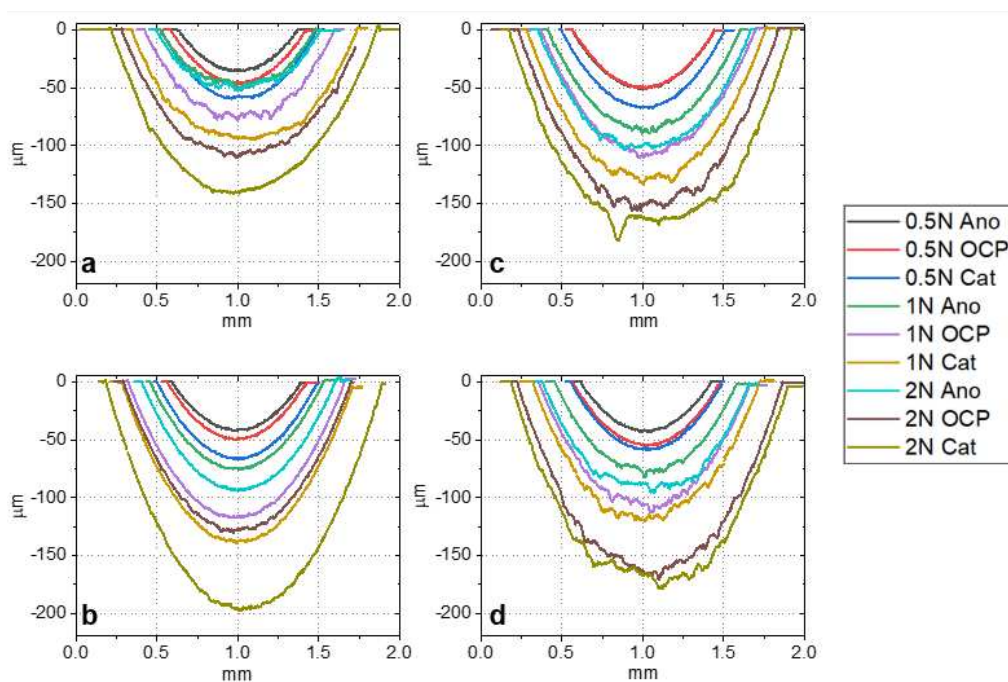


Fig. 6 – (a) Wear track profile $\alpha\beta$ alloy, (b) wear track profile $N\beta$ alloy, (c) wear track profile β alloy and (d) wear track profile $\beta\omega$ alloy.

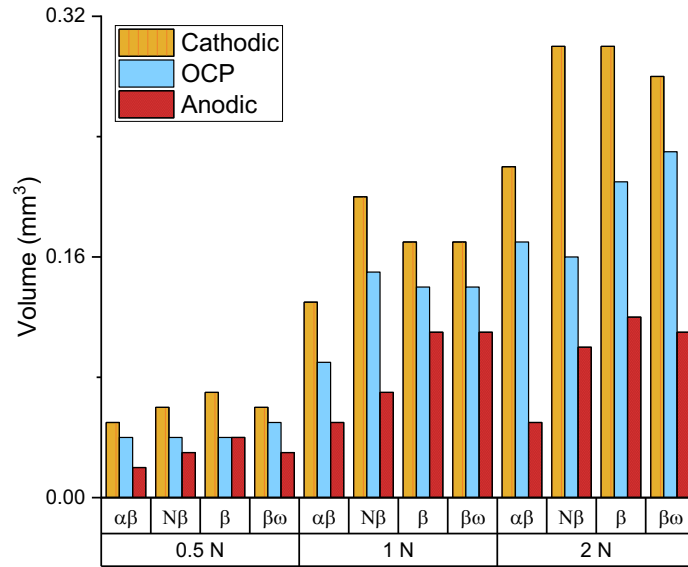


Fig. 7 – Wear track volume.

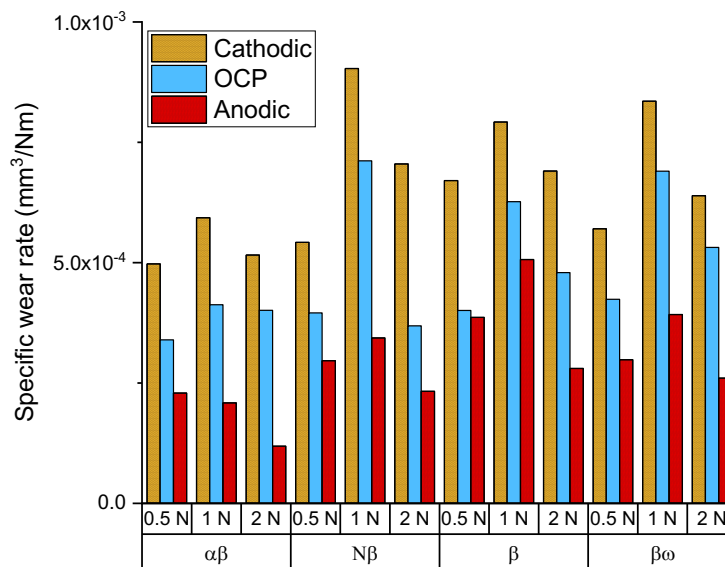


Fig. 8 – Specific wear rate.

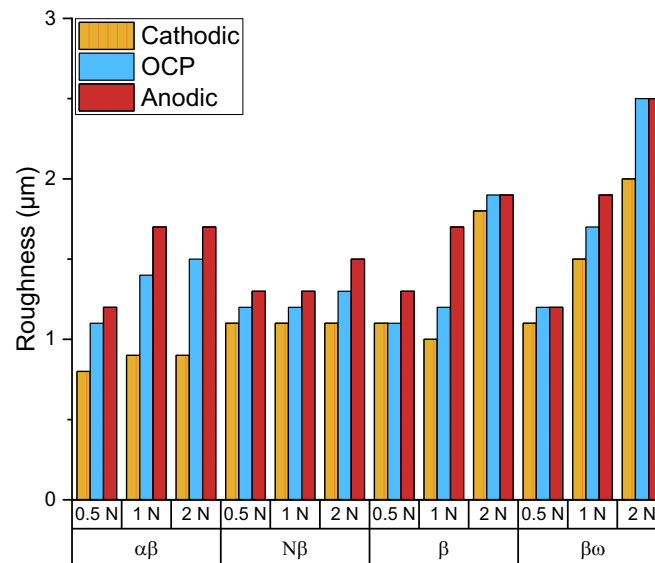


Fig. 9 – Roughness of wear track.

Synergy estimations

Synergy estimations according to synergistic approach and mechanistic approach were in agreement. Mechanical wear was the main cause of material loss and it increased with normal load and anodic potential (Fig. 10). In fact, chemical wear was only observed in low values at anodic potential.

The synergistic approach, Fig. 11, also showed that material loss due to wear (W_o) is the main cause of material loss. The corrosion portion W_c was negative, indicating a beneficial effect by inhibiting material loss.

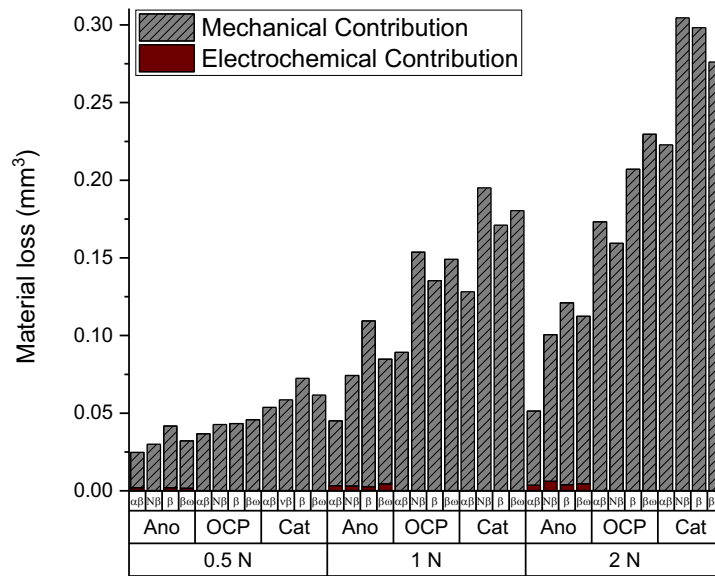


Fig. 10 – Mechanism approach.

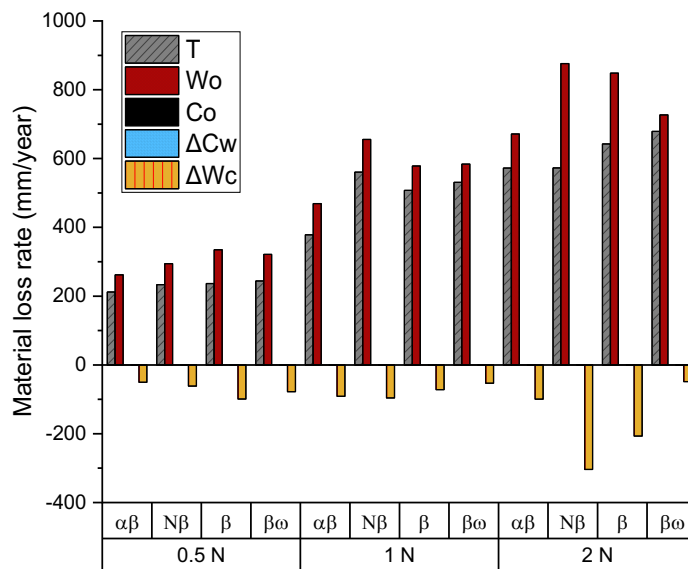


Fig. 11 – Synergistic approach.

Discussion

It was the goal of this study to explore alternative titanium implant alloys and to characterize their tribocorrosion behaviour. All four alloys exhibited distinctly different

microstructures, especially with respect to phase content, whereas the grain size was comparably small. It is clear that normal load had great impact on material loss. However, it is not the only important parameter. Alloy microstructure also has a notable influence where the presence of alpha phase is likely to lower material loss. Interestingly, these titanium alloys experienced lower material loss at anodic potential which is characteristic of an antagonistic behaviour. These main topics are discussed in the next paragraphs.

Tribocorrosion behaviour

In general, at cathodic potential, the current dropped after sliding started in all cases and it is due to proton reduction. This is caused by mechanical action and the enhancement of the cathodic reaction rate caused by the stirring of the electrolyte in the tribocell which affects the kinetics of mass transport. The main cathodic reactions proposed at this potential may be the oxygen reduction: $O_2 + 2H_2O + 4e^- \rightarrow 4OH^-$.

The constant value of OCP during sliding is linked to the dynamical equilibrium of depassivation and repassivation. The potential drops when sliding started, due to the exposure of a bare metal and it suggests this alloy becomes active as a result of the sliding. This reflects the galvanic coupling of two distinct surfaces states that are unworn area (cathodic area) and worn area (anodic area), which was stabilised. The constant value of OCP during sliding is attributed to the dynamic equilibrium between mechanical depassivation and electrochemical repassivation. When sliding stopped, a parabolic anodic shift was observed indicating a non-instantaneous repassivation.

Other studies [26] have shown that Ti alloys become more active under tribological conditions. Zavieh [27] studied the effect of friction on tribocorrosion behaviour of stainless steel. It was found that at OCP, the potential dropped when sliding started suggesting a high depassivation rate and galvanic coupling between the unworn (passivated) area outside the wear track and the fresh (depassivated) area due to sliding of the counterpart. This is a typical behaviour of passive alloys.

The current increased when sliding at anodic potential due to the removal of the passive film and exposure of bare and active material to the electrolyte in the contact region. It led to a reaction between the active exposed surface and the electrolyte accelerating the electrochemical reaction and anodic metal oxidation (metal dissolution) since the passive film acts as a charge barrier [28]. Guadalupe [29] applied

anodic polarization on CoCr alloys with different carbide contents and observed that the wear test at anodic potential showed an increase of current when sliding started and attributed it to the enlargement of the wear track with progressing wear. Also, another study reported that COF is lower at anodic potentials for CoCrMo and 316L stainless steel in bovine serum and H₂SO₄ [30, 31]. The lower COF at anodic potential has also been identified in a study of tribocorrosion behaviour of Ti6Al4V in artificial seawater at low contact pressures [32] and for stainless steel in H₂SO₄ solution [33]. Diomidis [34] studied the surface state behaviour of complex metallic alloys in sliding contacts and observed the dependence of COF to electrochemical condition in PBS.

The low mean COF and material loss at anodic potential could be explained by the presence of a tribofilm which acts as a lubricant. This was reported by Liao [35] which studied the graphitic tribological layers and concluded that transition metals remove water and ammonia from albumin which leads to a formation of a layer used to reduce friction.

There is no significant difference on potential, current and COF evolution among these alloys. The average COF increases with normal load at cathodic potential and OCP and remained unchanged with normal load at anodic potential. However, cathodic potential always shows larger values while anodic potential shows lower values. The low COF of the $\alpha\beta$ alloy is attributed to the presence of α phase which is harder than the β phase. The limited plastic deformability of α phase is explained by its number of slip systems. In fact, α phase is a hexagonal close packed phase and it has only 3 slip systems, while β phase (bcc) has 12 slip systems. It is clear that COF increases with normal load at OCP and cathodic potential and remains unchanged at anodic potential.

Synergy estimations

Material loss due to corrosion (C_w) is low because these are passive metals and wear-accelerated corrosion (ΔC_w) is higher than C_w so it suggests that wear enhanced corrosion rate. However, corrosion-accelerated wear (ΔW_c) showed negative values and all components increased with normal load, called negative synergism or antagonistic effect. The negative values observed on corrosion-accelerated wear suggests that corrosion does not accelerate wear rate. In fact, it

reduces wear rate and a positive effect of corrosion on wear that reduces friction is observed. This might be explained by presence of a lubricant and this might be why wear track volume at anodic potential show lower values. It changes the contact stress field where the effect of friction is reduced.

Numerous studies, some listed in the next paragraphs, have found systems to have negative synergistic effects or antagonistic effect. This might be explained by the reactions of organic species and particles that create a self-healing film on worn surface.

Albayrak [36] compared the tribocorrosion behaviour of CP titanium to duplex treated CP titanium and nitrided CP titanium in simulated body fluid. It was found that all alloys tested have an antagonistic effect behaviour and it was stronger on the nitride specimens. It was attributed to solution formed oxide layer on the surface of the alloys.

Hodge [37] studied the tribo-corrosion mechanisms of 316L stainless steel in soft drinks. It was observed that medium loads and higher viscosities produce synergistic conditions whilst combinations of either high loads and low viscosities or low loads and high viscosities produce antagonistic conditions. It was stated that 316L stainless steel in both milk and soda experience antagonistic and transition regimes for the majority of loads tested due to the formation of protective passive films in the anodic regime. Also that corroded metals ions may alter the solution viscosity which will in turn have an effect on the contact friction coefficient.

Sadiq [38] studied the behaviour of CoCrMo alloy in calf serum solution in a wide range of normal load and potentials. The CoCr alloys showed an antagonistic effect when SiC particles are present in the electrolyte. The antagonistic effect was attributed to the accumulation of organic material on the alloy surface. Also, it was pointed out that the antagonistic effect may be a result of an increased solution viscosity, improving the lubrication regime and thus inhibiting corrosion–wear due to the mixed protein molecules and particles and that the hard SiC particles are likely to have embedded on the surface of the softer UHMWPE ball.

The analysis of the micro-abrasion–corrosion of a CoCrMo alloy in Ringer's solution show that antagonistic effects was also observed for the MoM and anodically polarised contacts [39].

A study with UNS S31603 and S32760 stainless steels show that they experienced an antagonistic effect while S30403 does not in NaCl solution. It was attributed to a reflection of the differences in repassivation kinetics or composition of the passive films reducing the overall level of two-body abrasion with S30403 having weaker repassivation/passive oxide film structure [40].

Conclusion

- The microstructure does have an effect on tribocorrosion behaviour of titanium alloys. The presence of α phase, a hard phase, is linked to lower material loss. However, the electrochemical condition plays the most important role since at anodic potential titanium alloys show an improvement of wear properties and lower material loss.
- Mechanical wear is the main cause of material degradation. It was identified that wear accelerates corrosion rate, but corrosion does not accelerate wear rate. In fact, corrosion deaccelerate wear rate - antagonistic behaviour – for this tribocorrosion system.

References

1. Rack, H., *et al.*, *Titanium alloys for biomedical applications*. Materials Science and Engineering: C, 2006. **26**(8): p. 1269-1277.
2. Long, M., *et al.*, *Titanium alloys in total joint replacement--a materials science perspective*. Biomaterials, 1998. **19**(18): p. 1621-39.
3. Chen, Q., *et al.*, *Metallic implant biomaterials*. Materials Science and Engineering: R: Reports, 2015. **87**: p. 1-57.

4. Goldberg, J.R., et al., *The electrochemical and mechanical behavior of passivated and TiN/AlN-coated CoCrMo and Ti6Al4V alloys*. *Biomaterials*, 2004. **25**(5): p. 851-864.
5. Barril, S., et al., *Influence of fretting regimes on the tribocorrosion behaviour of Ti6Al4V in 0.9 wt.% sodium chloride solution*. *Wear*, 2004. **256**(9-10): p. 963-972.
6. Pourzal, R., et al., *Alloy microstructure dictates corrosion modes in THA modular junctions*. *Clinical Orthopaedics and Related Research*®, 2017. **475**(12): p. 3026-3043.
7. Gnanavel, S., et al., *Electrochemical Behavior of Biomedical Titanium Alloys Coated with Diamond Carbon in Hanks' Solution*. *Journal of Materials Engineering and Performance*, 2018. **27**(4): p. 1635-1641.
8. Morlock, M.M., et al., *Head taper corrosion causing head bottoming out and consecutive gross stem taper failure in total hip arthroplasty*. *The journal of arthroplasty*, 2018. **33**(11): p. 3581-3590.
9. Banerjee, S., et al., *Gross trunnion failure after primary total hip arthroplasty*. *The Journal of arthroplasty*, 2015. **30**(4): p. 641-648.
10. Bansal, T., et al., *Gross trunnion failure in metal on polyethylene total hip arthroplasty—a systematic review of literature*. *International Orthopaedics*, 2020: p. 1-13.
11. Bolarinwa, S.A., et al., *Gross trunnion failure after a metal-on-polyethylene total hip arthroplasty leading to dissociation at the femoral head-trunnion interface*. *Arthroplasty today*, 2019. **5**(1): p. 5-10.
12. Martin, A.J., et al., *Role of corrosion in taper failure and head disassociation in total hip arthroplasty of a single design*. *Journal of Orthopaedic Research*®, 2018. **36**(11): p. 2996-3003.
13. Yang, X., et al., *Corrosion-wear of beta-Ti alloy TMZF (Ti-12Mo-6Zr-2Fe) in simulated body fluid*. *Acta Biomater*, 2016. **42**: p. 429-439.
14. Holzwarth, U., et al., *Total hip arthroplasty*. Brussels: European Commission, 2012.
15. Geetha, M., et al., *Ti based biomaterials, the ultimate choice for orthopaedic implants—a review*. *Progress in materials science*, 2009. **54**(3): p. 397-425.
16. Rodrigues, D.C., et al., *Titanium corrosion mechanisms in the oral environment: a retrieval study*. *Materials*, 2013. **6**(11): p. 5258-5274.
17. Ganesh, B.K.C., et al., *Dry sliding wear behavior of Ti-6Al-4V implant alloy subjected to various surface treatments*. *Transactions of the Indian Institute of Metals*, 2012. **65**(5): p. 425-434.
18. Bartolomeu, F., et al., *Multi-material Ti6Al4V & PEEK cellular structures produced by Selective Laser Melting and Hot Pressing: A tribocorrosion study targeting orthopedic applications*. *Journal of the mechanical behavior of biomedical materials*, 2019. **89**: p. 54-64.
19. Hatem, A., et al., *Tribocorrosion behavior of DLC-coated Ti-6Al-4V alloy deposited by PIID and PEMS+ PIID techniques for biomedical applications*. *Surface and Coatings Technology*, 2017. **332**: p. 223-232.
20. Tang, X., et al., *Phase transformations in Ti-Nb-Ta and Ti-Nb-Ta-Zr alloys*. *Journal of Materials Science*, 2000. **35**(7): p. 1805-1811.
21. Afonso, C.R.M., et al., *Influence of cooling rate on microstructure of Ti-Nb alloy for orthopedic implants*. *Materials Science and Engineering: C*, 2007. **27**(4): p. 908-913.
22. Afonso, C.R., et al., *High resolution transmission electron microscopy study of the hardening mechanism through phase separation in a beta-Ti-35Nb-7Zr-5Ta alloy for implant applications*. *Acta Biomater*, 2010. **6**(4): p. 1625-9.
23. Ferrandini, P.L., et al., *Aging response of the Ti-35Nb-7Zr-5Ta and Ti-35Nb-7Ta alloys*. *Journal of Alloys and Compounds*, 2007. **433**(1-2): p. 207-210.
24. ASTM, *G119 - 09(2016): Standard Guide for Determining Synergism Between Wear and Corrosion*. 2016: West Conshohocken, PA, USA: ASTM International.
25. Mischler, S., et al., *Effect of Corrosion on the Wear Behavior of Passivating Metals in Aqueous. Thin Films in Tribology*, 1993. **25**: p. 245.

26. Huang, W., et al., *Wear and Electrochemical Corrosion Behavior of Biomedical Ti–25Nb–3Mo–3Zr–2Sn Alloy in Simulated Physiological Solutions*. *Journal of Bio-and Tribo-Corrosion*, 2015. **1**(1): p. 1.
27. Zavieh, A.H., et al., *The effect of friction modifiers on tribocorrosion and tribocorrosion-fatigue of austenitic stainless steel*. *Tribology International*, 2017. **111**: p. 138-147.
28. Mischler, S., et al., *Wear of CoCrMo alloys used in metal-on-metal hip joints: a tribocorrosion appraisal*. *Wear*, 2013. **297**(1-2): p. 1081-1094.
29. Guadalupe, S., et al., *Applicability of a recently proposed tribocorrosion model to CoCr alloys with different carbides content*. *Wear*, 2017. **376**: p. 203-211.
30. Favero, M., et al., *Effect of the applied potential of the near surface microstructure of a 316L steel submitted to tribocorrosion in sulfuric acid*. *Journal of Physics D: Applied Physics*, 2006. **39**(15): p. 3175.
31. Yan, Y., et al., *Biotribocorrosion of CoCrMo orthopaedic implant materials—assessing the formation and effect of the biofilm*. *Tribology international*, 2007. **40**(10-12): p. 1492-1499.
32. Pejaković, V., et al., *Tribocorrosion behaviour of Ti6Al4V in artificial seawater at low contact pressures*. *Tribology International*, 2018. **119**: p. 55-65.
33. Sun, Y., et al., *Effect of electrochemical potential on tribocorrosion behavior of low temperature plasma carburized 316L stainless steel in 1 M H₂SO₄ solution*. *Surface and Coatings Technology*, 2011. **205**(17-18): p. 4280-4290.
34. Diomidis, N., et al., *Assessment of the surface state behaviour of Al₇₁Cu₁₀Fe₉Cr₁₀ and Al₃Mg₂ complex metallic alloys in sliding contacts*. *Intermetallics*, 2009. **17**(11): p. 930-937.
35. Liao, Y., et al., *Graphitic tribological layers in metal-on-metal hip replacements*. *Science*, 2011. **334**(6063): p. 1687-1690.
36. Albayrak, Ç., et al., *Tribocorrosion behavior of duplex treated pure titanium in simulated body fluid*. *Wear*, 2013. **302**(1-2): p. 1642-1648.
37. Hodge, C., et al., *Tribo-corrosion mechanisms of stainless steel in soft drinks*. *Wear*, 2010. **270**(1-2): p. 104-114.
38. Sadiq, K., et al., *Wear mapping of CoCrMo alloy in simulated bio-tribocorrosion conditions of a hip prosthesis bearing in calf serum solution*. *Materials Science and Engineering: C*, 2015. **49**: p. 452-462.
39. Sinnett-Jones, P.E., et al., *Micro-abrasion–corrosion of a CoCrMo alloy in simulated artificial hip joint environments*. *Wear*, 2005. **259**(7-12): p. 898-909.
40. Bello, J.O., et al., *Synergistic effects of micro-abrasion–corrosion of UNS S30403, S31603 and S32760 stainless steels*. *Wear*, 2007. **263**(1-6): p. 149-159.